Supporting Information for:

The Importance of Salt-Enhanced Electrostatic Repulsion in Colloidal Crystal Engineering with DNA

Soyoung E. Seo,[†,§] Martin Girard,[‡,α] Monica Olvera de la Cruz,[*,†,‡,§,α] and Chad A. Mirkin[*,†,‡,§]

Departments of [†]Chemistry, [‡]Materials Science and Engineering, [§]International Institute for Nanotechnology, and [α]Physics and Astronomy, Northwestern University, Evanston, IL 60208

*Address correspondence to: chadnano@northwestern.edu and m-olvera@northwestern.edu

This PDF file includes:

SI Materials and Methods

Molecular Dynamics Simulations:

Effective pair potentials, including electrostatic repulsion and short-range attraction between nanoparticles, were calculated *via* molecular dynamics (MD) simulations to study the crystallization of charged nanoparticles. In previous studies, colloidal models were extended to predict the shape of grains of DNA-coated nanoparticle crystals.[1] Here, MD simulations were carried out to understand the change in interaction between nanoparticles as the salt concentration is increased above the regime where the Debye-Hückel theory is valid. These calculations were not done under 0.3 M NaCl since previous results show that DLVO-type potentials with renormalized charge are a good description for ionic behavior.[2] This has been experimentally verified by measuring interparticle distances of DNA-coated nanoparticles with a proposed mean-field model that correlates well with existing theories.[3]

The 3SPN DNA Model

The DNA model that we used previously[4] is not detailed enough to provide attachment barriers, which are critical in nucleation theory. Therefore, we turn to the 3SPN model developed by the de Pablo group.[5-6] The model uses three beads per nucleotide located at phosphates, sugars, and bases. The charge (-1e) is carried by the phosphate bead while ions have charges of +1e (Na) and -1e (Cl). The permittivity of water is set to 78.5. The ion-ion interactions are tabulated potentials[6] and are available at https://github.com/groupdepablo/USER-3SPN2. Since the ions are coarse-grained from atomistic simulations, they should reproduce clustering behavior found in a previous study.[7]

The bonded interactions include dihedrals to reproduce B-form DNA helix conformation. The model implements base specific interactions for base-pairing, base-stacking, and cross-stacking. The excluded volumes were treated by Weeks-Chandler-Anderson potentials. The electrostatic calculations used a damped shifted force with a cutoff of 30 Å and a damping constant of 0.01 $Å^{-1}$.[8] The values of cutoff and damping constant were not found to strongly affect the total electrostatic energy of the system.

We used a custom implementation of the potentials in the HOOMD-blue engine to perform calculations on GPU.[9-10]

Calculating Potential of Mean Force for DNA-Coated Nanoparticles

Initial configurations were generated using HOOBAS,[11] which uses X3DNA software.[12] The simulation size is set to $d_x = d_y = 60$ nm for the x- and y-dimensions and $d_z = 120$ nm for the z-dimension. Simulations were carried out in the canonical ensemble using Langevin dynamics with a drag coefficient γ of the i^{th} particle, which was set to $\gamma_i = \sigma_i/2$ (σ_i is the diameter of the i^{th} particle). These coefficients were chosen to be smaller than the value expected from the Stokes law and water dynamical viscosity for numerical equilibration times. With this setup, simulations contain up to $3.85*10^5$ ions. The nanoparticles were constrained to move along the z-direction only. An additional spring was added between two nanoparticles with potential energy $U_{bias} = K_{bias}\,(z - z_0)^2$, with $K_{bias} = 0.25$ kJ/mol/$Å^2$. Each simulation was run at a given value of z_0 which represents one window for umbrella sampling. Each window was sampled at $5*10^6$ timesteps of $\Delta t = 0.07\ \delta t$, where δt is the time unit (approximately equal to $1*10^{-13}$ s). Windows were separated by at most 3 Å. In the barrier region around 380 Å, the potential of mean force was sampled more finely with the distance between windows to be around 1 Å. The final potential is reconstructed by Multistate Benett Acceptance Ratio (MBAR) method in the molecular analysis package from the Computational Biophysics Research Team at RIKEN (http://www.riken.jp/TMS2012/cbp/en/research/software/index.html, package available online:

https://github.com/ymatsunaga/mdtoolbox). The potential energy calculations for a larger range of distances were restricted due to limited computational resources.

An additional biasing potential was added between complementary sticky ends. This biasing takes the form of a Morse potential:

$$U_{Morse} = D_e\left(1 - \exp\left(-\alpha(r - r_0)\right)\right)^2 - D_e \quad \text{Eq. S1}$$

with α = 0.33 Å^{-1}, D_e = B 2.65 kJ/mol for G-C pair, and D_e = B 4.18 kJ/mol for A-T pair. The quantity B is the amount of biasing introduced in the simulation. We used Hamiltonian replica exchange to exchange configurations between 4 different replicas that have B = 0, 0.5, 1 and 1.5 to overcome the long diffusion time between two complementary sticky ends finding each other. The system was equilibrated for $3*10^4$ timesteps after each swap. The data for the potential of mean force was gathered over $5*10^4$ timesteps before another swap attempt was made. Swapping probabilities vary from ~30% for close separations up to 100% for large separations as the biasing force only acts between complementary linker strands.

Crystal growth

To calculate crystal growth kinetics, we turn to classical nucleation theory. These equations are valid as long as there are no strong concentration gradients and crystals grow in a dilute regime. The actual experiments are conducted using a slow cooling approach where equilibrium Wulff shapes are observed. The formation of Wulff crystals indicates that the concentration gradients are weak and thus the assumptions based on classical nucleation should be valid. Nevertheless, experiments do show the formation of some fused single crystals, suggesting the presence of a coalescence mechanism (see below). However, based on the high proportion of well-defined rhombic dodecahedra, we assume that this effect is weak and slow relative to crystal growth.

The model assumes that the value of ΔG' is directly transferable from the potential of mean forces to a crystal, neglecting any multi-body interactions and second nearest neighbor interactions. The attachment barrier occurs at distances relatively large compared to the equilibrium interparticle spacing and the distance to the second nearest neighbor, and thus we can disregard such interactions.

The number of crystals growing at any point, k, increases at a rate given by:

$$\frac{dk}{dt} = jexp(\frac{-16\pi\gamma^3}{3\Delta\mu^2}) \quad \text{Eq. S2}$$

where γ is the surface energy, $\Delta\mu$ is the chemical potential given by $\Delta\mu = \Delta\mu_0 + \log(c/c_0)$, where c is the current concentration and $\Delta\mu_0$ is the drive at concentration c_0. We assumed the Zeldovitch factor to be 1. For simplicity, we assume that the surface energy is isotropic. An anisotropic surface energy would alter the volume-to-surface ratio and rescale the overall chemical potential drive in Eq. S2. Adding this factor would displace the plateau region in Fig. 1C but leave the curve shape unchanged. Two different rates of crystal growth can be derived. In interface-limited regimes, the growth rate of the number of atoms of the i^{th} crystal is given by:

$$\frac{dn_i}{dt} = j\Delta\mu n_i^{2/3}\tau \quad \text{Eq. S3}$$

where τ is the proportionality constant and n_i is the number of atoms in the i^{th} crystal. In diffusion-limited regimes, the growth rate is given by:

$$\frac{dn_i}{dt} = 3V_m \Omega D n_i^{1/3} \quad \text{Eq. S4}$$

where Ω is the supersaturation given by $\Omega = (c - c_{eq})$ for spherical particles, c_{eq} is the equilibrium concentration, V_m is the molar volume, and D is the diffusion constant. For small values of n_i, the growth is interface-limited while for the large values of n_i, the growth is diffusion-limited. While one would generally assume a mixture of rates when the growth is neither limited by diffusion or interface, in this study, we assumed that the growth rate is at its minimum of the diffusion or interface-limited rates. The evolution of concentration of the solution is given by:

$$\frac{dc}{dt} = -\sum_i^k \frac{dn_i}{dt} \times \frac{1}{V} \quad \text{Eq. S5}$$

where V is the total volume. Since numerical integration requires the number of dimensions of the differential equations to be an integer, we used stochastic integration for Eq. S1. During a timestep, the probability of increasing the number of dimensions by one (forming a new nuclei) is given by:

$$\mathrm{P(k+1)} = \Delta \mathrm{t} \times \mathrm{jexp}(\frac{-16\pi\gamma^3}{3\Delta\mu^2}) \quad \text{Eq. S6}$$

where $\Delta t = 0.001$ is the size of a time step. This implicitly discards any chances of having two or more nucleation events occurring in the same timestep. In the case a nuclei forms, we assumed that it is of a critical size, $n_c = (2\gamma/\Delta\mu)^3$. The number of atoms in the i^{th} nuclei was integrated using the following equation:

$$\frac{dn_i}{dt} = \min(j\Delta n_i^{2/3}\tau, 3V_m \Omega D n_i^{1/3}) \quad \text{Eq. S7}$$

This equation assumes that the growth rate is at its minimum between the interface-limited and diffusion-limited regimes. Usually, an additional contribution is added to $\Delta\mu$ from the surface tension which results in Ostwald ripening. We ignored this type of contribution in our calculations for two reasons. First, this process is extremely slow and is not seen in timescales at which crystallization occurs in molecular dynamics.[13-14] Second, Ostwald ripening results in a distribution with a negative skew, which is inconsistent with experimental results. Therefore, for numerical simulations, we used $\tau = 3$, $V_m \mathrm{D} = 0.05$, $V = 10^8$, $c_0 = 1$, $\Delta\mu_0 = 2$, and $\gamma = 2$. The changes in these values result in different quantitative, but similar qualitative, behavior.

Coalescence

In previous work on DNA-mediated assemblies, it has been shown that crystals assembled with PAEs can grow by coalescence.[13] We included coalescence in our simulations by assuming that the probability of the i^{th} and j^{th} crystals coalescencing during a timestep is: $P(\mathrm{coal}) = \Delta t\, k_{coal}\, (D_i + D_j)$, where k_{coal} is the rate of coalescence and D_i is the diffusion constant of crystal i, which we assumed to follow Stokes equation $D_i = 1/n_i^{1/3}$. When two crystals coalesce, we assumed that they instantly equilibrate to a spherical shape with $n_i = (n_i + n_j)$ and $n_j = 0$. While not entirely physical, it produces reasonable results when k_{coal} is low and the surface diffusion of the PAE is sufficiently large. Realistically, this is only valid when small crystals coalesce with either small or large crystals. Two large crystals coalescing together would lead to quenched structures. It is possible that the system undergoes simultaneous Ostwald ripening

and coalescence, a process which requires a delicate treatment of the actual geometry of individual crystals. Nevertheless, we included results based on this approximation in the SI since they reproduce experimental distribution skew.

Size Distributions

The distribution of crystal size is an interesting quantity to compare simulations to experiments. Distributions generated with $k_{coal} = 0$ provide ones with mostly negative skew (Fig. S1). For crystals *via* nearly fully interface-limited growth, the skew is small. However, crystals grown mostly in the diffusion-limited regimes show highly negative skew. For instance, using an attachment rate of 0.0016, we find a skew of -0.16, whereas an attachment rate of 0.54 shows a skew of -0.67. Neither of these distributions exhibited a positive skew and doubly-peaked distributions observed in experiments (Fig. 2C-E).

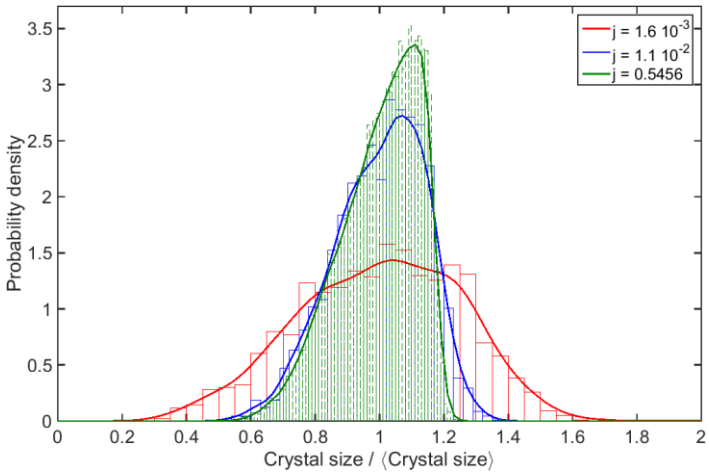

Figure S1. The distribution of normalized crystal size for attachment rates of 0.0016, 0.011 and 0.55. The evolution towards a narrow negative-skew distribution with increasing attachment rate is observed. Histogram is obtained from raw data while the curves were estimated from the kernel density estimation.

Setting a non-zero value to k_{coal} produces interesting results. For sufficiently low values of k_{coal}, we observe an initial growth phase followed by a coarsening phase (Fig. S2). When coarsening occurs during the crystallization, the distribution exhibits 2 maxima akin to what is observed in experiments. The simulations show that the skewness drops during initial growth but increases during coarsening. Eventually, it reaches a value slightly above 1.5, even for systems with high attachment rates.

This would suggest that some coarsening of crystals occur in our experiments. However, the coarsening process is typically very slow. Moreover, TEM images show quenched, coalesced crystals, which were ignored in our statistics. This is in agreement with prediction from previous simulations,[13] which were calculated at finite undercooling. It is difficult to determine whether the quenched states observed on TEM images were created during slow cooling process at elevated temperature *via* coalescence events or afterwards. Furthermore, elevated melting temperature at higher ionic strength could hypothetically promote higher diffusion on crystal surfaces and favor the relaxation of coalesced crystals.

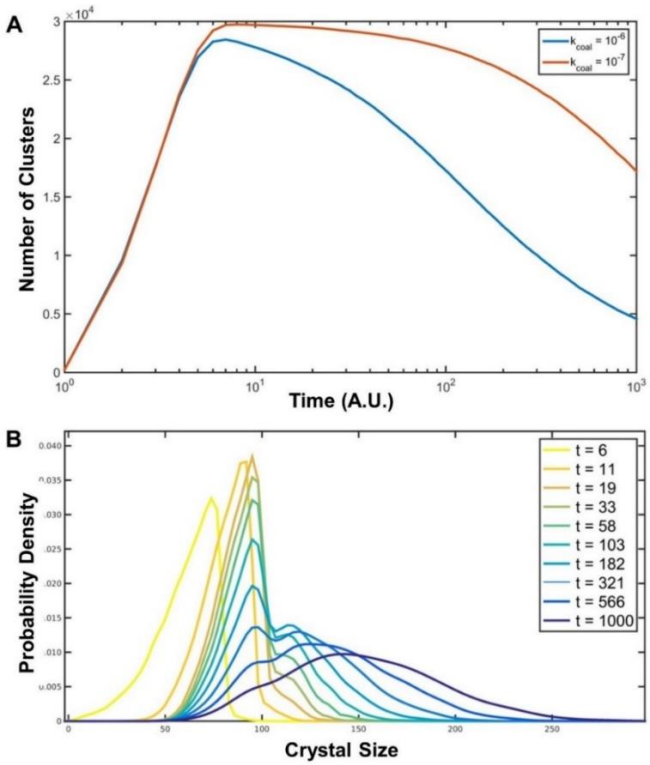

Figure S2. (**A**) The number of crystals as a function of time for two values of k_{coal}, clearly showing the initial growth and subsequent coarsening. (**B**) The distribution of crystal sizes during the coarsening with $k_{coal} = 10^{-6}$ for different times. The curve shows a second peak for intermediate times. Attachment rate is set to 0.5456.

DNA Synthesis and Purification:

All oligonucleotides were synthesized on a solid-support MM48 synthesizer (Bio Automation) with reagents purchased from Glen Research. DNA strands were synthesized with a 5' trityl group (hydrophobic) and purified by reverse-phase high-performance liquid chromatography (HPLC; Agilent), followed by standard deprotection protocols.[3] Six different types of DNA were synthesized in this work, two of which contained a 5' hexylthiol group. Because the 5' hexylthiol group is cleaved during the DTT step, the deprotection protocol to remove the acid-labile trityl group was skipped. All oligonucleotides were characterized by matrix-assisted laser desorption/ionization time-of-flight (MALDI-TOF) mass spectroscopy. DNA concentration was measured on a Cary 5000 UV-Vis-NIR spectrophotometer (Agilent) using extinction coefficients from the IDT OligoAnalyzer (https://www.idtdna. com/calc/analyzer). DNA sequences used in this study are listed in Table S1.

DNA-Functionalization and Assembly of Nanoparticles:

Nanoparticles were functionalized with 5' thiolated oligonucleotides (Anchor #1 and #2, Table S1) according to literature precedent.[15] Thiolated oligonucleotides were treated with a solution of 100 mM dithiothreitol (DTT) for 1 h, which was then purified using Nap-5 size exclusion column (GE Healthcare) to remove remaining DTT. Deprotected oligonucleotides were immediately added to a Au nanoparticle solution in a ratio of approximately 6 nmol of DNA per 1 mL of Au colloid, followed by addition of the surfactant sodium dodecyl sulfate (SDS) to bring the final surfactant concentration to 0.01 *vol*%. Initial addition of the purified thiol-modified DNA allows the formation of a low-density monolayer of oligonucleotides on the nanoparticle's surface. The DNA loading was increased using a "salt aging"

process,[16] where 5 M NaCl solution was slowly added over the course of a few hours to bring the final NaCl concentration of 0.5 M. In between each addition of salt, the solution was vortexed and sonicated for a few seconds. After bringing the final NaCl concentration of 0.5 M, the Au nanoparticles were incubated in a shaker overnight at 37°C at 130 rpm. Unbound DNA, excess salt, and surfactant were removed by three rounds of centrifugation in 100 kDa membrane filter centrifuge tubes (Millipore) on a swinging bucket centrifuge (2,200 rpm) and then suspended in Nanopure water (18.2 MΩ, Millipore). After DNA functionalization, nanoparticle concentration was quantified on a Cary 5000 UV-Vis spectrophotometer using known extinction coefficients from the Ted Pella website (http://www.tedpella.com/gold_html/gold-tec.htm).

To each colloid, 400 linker strands were added per nanoparticle (in slight excess of the number of thiolated strands). After the addition of linker to each nanoparticle solution, samples were prepared such that the final concentration of NaCl was either 0.3, 0.5, or 1 M, and of each sample was 30 nM in a total volume of 100 μL. Each solution was then transferred to 200 μL PCR tubes (Applied Biosystems) and placed into a thermal cycler (Life Technologies). The temperature of the thermal cycler was heated up to 55°C (where particles are fully discrete) and slowly cooled to 25°C (where nanoparticles are fully associated) at a rate of 0.1°C/10 min. The slow temperature gradient ensures that nanoparticles have sufficient time to assemble to form faceted single microcrystals. The melting temperature was determined by taking the derivative of the melting curves and finding the *x*-value corresponding to the maxima. The full slow cooling procedure took ~2-3 days.

Table S1. DNA Sequences Used to Assemble Nanoparticles.

Name	E_{260}, $M^{-1}\cdot cm^{-1}$	MW, g/mol	Sequence (5' to 3')
Anchor #1	164,100	7,404	HS-$(sp18)_5$-CAT CCA TCC TTA TCA ACT
Anchor #2	170,200	7,438	HS-$(sp18)_5$-AAC GAC TCA TAC TCA CCT
Linker 6SE #1	239,000	7,782	TT CC TT-(sp18)-AGT TGA TAA GGA TGG ATG
Linker 6SE #2	254,000	7,865	AA GG AA-(sp18)-AGG TGA GTA TGA GTC GTT
Linker 7SE #1	247,100	8,086	TT CC TTT-(sp18)-AGT TGA TAA GGA TGG ATG
Linker 7SE #2	266,000	8,178	AAA GG AA-(sp18)-AGG TGA GTA TGA GTC GTT

*One sp18 is equivalent to one hexaethylene glycol unit manufactured by Glen Research.

EM of Nanoparticle Superlattices:

Slow-cooled samples were transferred to 1.5 mL Eppendorf tubes, and the final volume was brought up to 1 mL with a solution at an appropriate salt concentration. To this solution, 2 μL of the quaternary silane salt, *N*-trimethoxysilylpropyl-*N*,*N*,*N*-trimethylammonium chloride (TMSPA), was added and the tube was mixed at room temperature (thermomixer, 700 rpm) for 30 min. After the TMSPA was allowed to electrostatically associate with the negatively charged DNA backbone, 4 μL of triethoxysilane (TES) was added to the solution and allowed to form a silica network around the entire lattice for four days. Each solution was then centrifuged and washed three times to remove excess reactants. These methods preserve the crystal symmetry and lattice parameters of the lattice but allow transition to the solid state for imaging. Note, the addition of water does not result in lattice dissolution (i.e., the solution does not turn red) in the case of successful silica embedding. It is often impossible to remove excess silica chunks, which often appear, during the purification process.

Scanning Electron Microscopy:

5 μL of each silica embedded sample was dropcasted onto a silicon wafer for imaging. SEM was used to characterize crystal morphology and determine the size distributions of each crystal population. All images were collected on a Hitachi SEM SU8030 at an accelerating voltage of 10 kV with either SE_L or BSE_L detectors at the Northwestern University Atomic and Nanoscale Characterization Experimental Center (NUANCE).

Transmission Electron Microscopy:

Microcrystals encapsulated in silica were embedded in a polymeric resin and microtomed into sections 80-300 nm thick (1 to 3 unit cells). Briefly, the silica embedded samples were embedded in EMbed-812 resin (Electron Microscopy Sciences) following standard protocols. First, samples were enrobed in 60 μL of liquefied 2 *wt*% agar and then were drawn up by a glass pipette and expressed into cold water in 1.5 mL Eppendorf tube. If the pallet solidified inside the pipette, dipping the pipette into warm water should liquefy the agar. The gelatin-superlattice was then dehydrated by ethanol substitution (30, 50, 70, 80, 90, and 100% chilled EtOH), repeating three times at each concentration for 15 min. It is crucial that each step is followed and completed. For the last dehydration step, the sample was transferred to neat acetone and incubated for 10 min, followed by infiltration with resin, 1:1 acetone:resin mixture for 1 h at 300 rpm then 1:2 acetone:resin mixture overnight at 300 rpm. The sample was transferred to a 100% activated resin (accelerant: benzyldimethylamine) for 6 h, which was then placed in the bottom of a BEEM capsule mold with activated resin mixture. This mixture was cured at 60°C for 48 h until the resin was completely polymerized. Thin sections of polymeric resin embedded samples allow one to evaluate the crystallinity within each crystal, which is difficult to analyze using SEM (SEM only provides information about nanoparticles on the surface and overall crystal morphology). All images collected for sectioned superlattices were collected on a Hitachi TEM HT7700 and a Hitachi STEM HD2300 in Z-contrast mode at NUANCE. The selected area diffraction was performed over large areas to qualitatively evaluate the crystallinity inside a TEM. The SAD diffraction patterns allow one to determine the crystal orientations of two-dimensional projections down the major symmetry axes.

Small Angle X-ray Scattering (SAXS):

SAXS experiments were performed at the DuPont-Northwestern-Dow Collaborative Access Team (DND-CAT) beamline of the Advanced Photon Source (APS) at Argonne National Laboratory. The data were collected with E = 10 keV and λ = 1.24 Å collimated X-rays calibrated with a silver behenate standard. Two sets of slits were used to define and collimate the beam and parasitic scattering was removed with a pinhole. X-ray beam cross-section of 200 μm and a 0.5 s exposure time were used. Longer periods of X-ray exposure damaged the crystals. Approximately 60 μL of the sample was loaded into a 1.5 mm quartz capillary (Charles Supper) and placed into a sample stage in the path of the X-ray beam. Dark current frames were subtracted from all data. Two-dimensional scattering data were collected on a CCD area detector and converted to one-dimensional data *via* radial averaging to generate plots of scattering intensity I(q) as a function of the scattering vector, q:

$$q = 4\pi \sin(\theta) / \lambda \qquad \text{Eq. S8}$$

where θ is the scattering angle and λ is the wavelength of the X-ray radiation. The scattering associated with gold relative to the DNA and solvent is the orders of magnitude different, therefore scattering from these sources was assumed to be negligible. I(q) includes scattering contributions from the discrete nanoparticles described as a form factor, P(q), and from lattice effects described as a structure factor, S(q). The structure factor is calculated using this relationship:

$$I(q) = \frac{S(q)}{P(q)} \quad \text{Eq. S9}$$

Full scattering profiles for crystalline assemblies were indexed by modeling patterns of ideal lattice structures generated using MATLAB. More detailed description about the peak fitting protocol can be found in literature.[17] All crystals in this study had a body-centered cubic (bcc) arrangement of spherical particles. Interparticle spacing (in nm), d_{Au}, for these crystals was determined from the position of the first order scattering peak, q_0. A value of C (= $\sqrt{(6)}\pi$) is a constant that correlates the distance between two nearest neighbors and the distance between the [*hkl*] planes (*e.g.*, [110]) associated with the scattering peak, and is used to calculate the lattice parameter.

$$d_{Au} = \frac{C}{10q_0} \quad \text{Eq. S10}$$

Williamson-Hall Peak Analysis:

S(q) for each sample was fit to Lorentzian profiles. The integral breadth of each peak (β) was used to determine average crystal domain sizes and apparent stress. Specifically, the Scherrer formula for size broadening combined with the Stokes-Wilson expression for strain broadening was used to establish the relationship between crystal domain size and microstrain:

$$\beta \cos(\theta) = \frac{k\lambda}{\tau} + \varepsilon \sin(\theta) \quad \text{Eq. S11}$$

where θ is the scattering angle, β is the integral breadth of the scattering peak, λ is the wavelength of X-ray radiation, τ is the crystal size in the direction perpendicular to the beam, ε is the apparent strain, and k is the shape factor, which is approximated as 0.9 for spherical crystallites. This can be rewritten as:

$$\beta^* = \frac{1}{D} + \varepsilon q \quad \text{Eq. S12}$$

where $\beta^* = \beta \cos(\theta/\lambda)$ and $q = 4 \sin(\theta/\lambda)$. Plotting β^* versus q should result in a straight line where ε is the slope, a, and $1/D$ is the intercept, b. The crystallite size was calculated based on the values determined from the plot in Fig. S6:

$$Crystallite\ Size = \frac{k\lambda}{10 * Asin(\lambda b/4\pi) * \cos(Asin(\lambda q_0/4\pi))} \quad \text{Eq. S13}$$

During peak fitting, factors from the instrument were not explicitly subtracted out. However, all sample peak widths were more than twice as broad as a standard silicon diffraction grating, and therefore, these factors are not expected to contribute substantially to peak broadening, and the trend observed herein should be unaffected. It is important to note that the average crystalline domain sizes calculated using this method account for the size in the direction perpendicular to the beam. Therefore, depending on the orientation of crystal that the beam travels through, the size does not represent the maximum length as measured in SEM images.

Melting Transition Determination:

The melting temperature of each sample was determined using an Agilent Cary 5000 UV-Vis spectrophotometer. An aliquot of disordered aggregate was diluted in 1 mL of buffer of the appropriate salt

concentration. Note that the overall absorbance at 520 nm is between 0.1 and 1.0 A.U. The sample was placed in a cuvette equipped with a magnetic stir bar. The extinction of the solution was monitored at 260 nm and 520 nm, while the thermal stage was heated from 25°C to 65°C at a rate of 0.1°C/min. The melting temperature was calculated from the point of inflection on the raw data (Fig. S4A) where there is a dramatic increase in the extinction as the nanoparticles dissociate above their melting temperature. Although the same protocol was followed for all samples, there was a slight variation in melting temperature for sample with the identical set of particles and conditions (*i.e.*, particle size, DNA sequence, salt concentration, and final sample volume) but prepared at different times. This is most likely due to slight deviations in DNA loading or aggregate size. Nonetheless, the trend of increasing melting temperature with salt concentration is observed.

SI Discussion

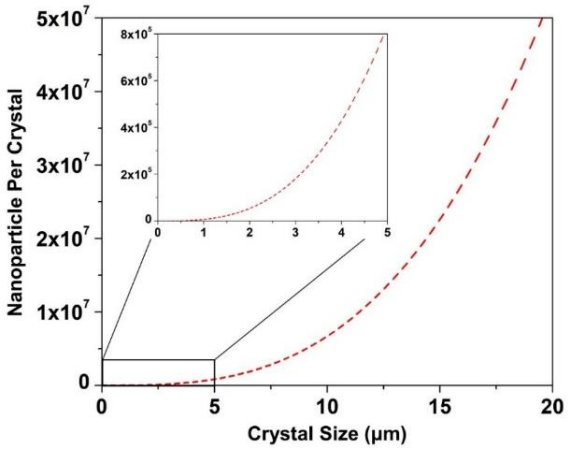

Figure S3. The number of nanoparticles within a crystal for a range of sizes was calculated based on the unit cell size and number of nanoparticles per unit cell (two nanoparticles in a bcc unit cell). The values shown here were solved mathematically.

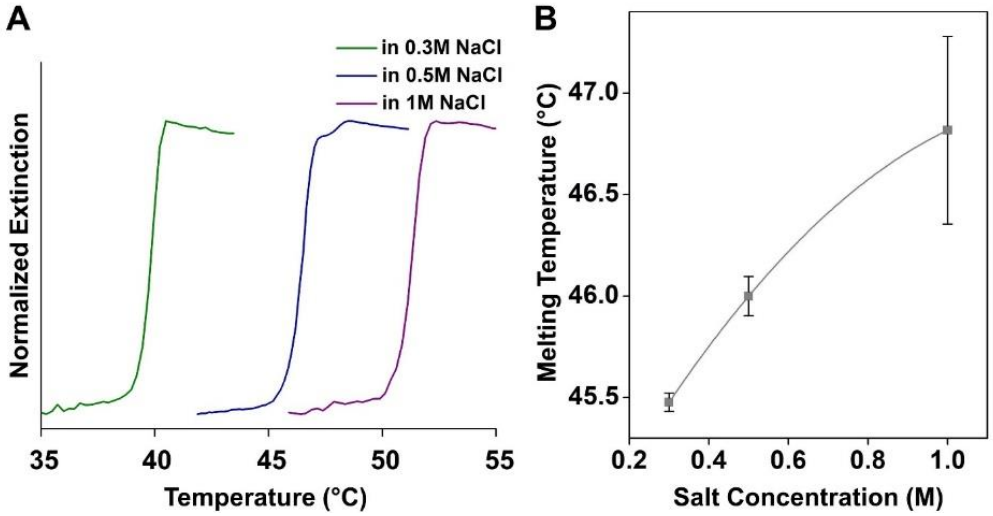

Figure S4. Melting temperatures of systems at different solution salt concentrations (0.3, 0.5, and 1 M) were determined as the largest value in the first derivative (**B**) of the melting curve (**A**). These values represent the melting temperature of unannealed aggregates (*e.g.*, disordered).

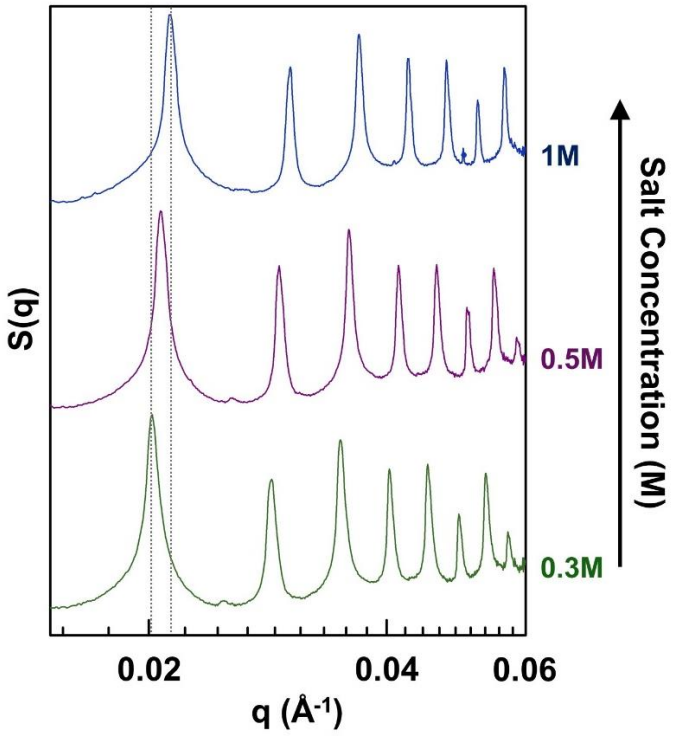

Figure S5. SAXS data for bcc superlattices of 15-nm nanoparticles at different NaCl concentrations.

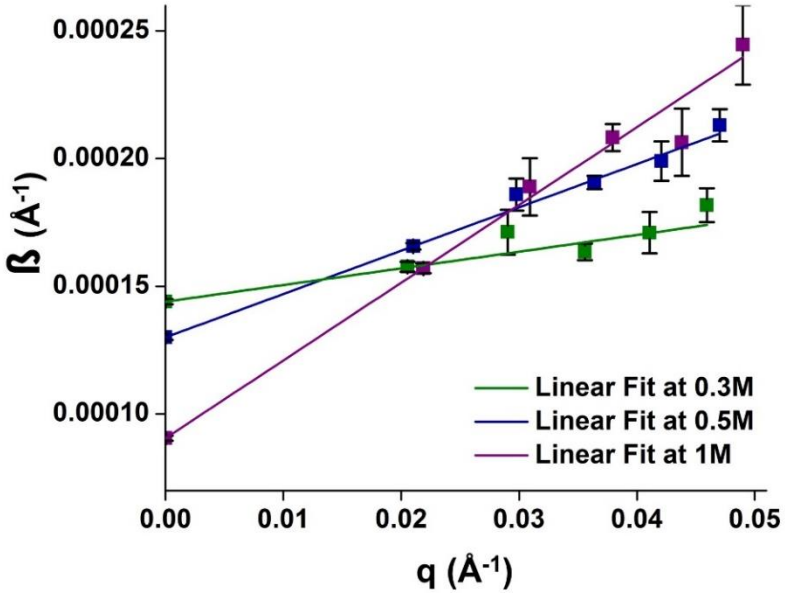

Figure S6. Representative results from the fitting protocol. Williamson-Hall analysis performed on SAXS patterns collected for microcrystals generated from three different salt concentrations (0.3, 0.5, 1 M NaCl). Linear fits are exhibited by all samples.

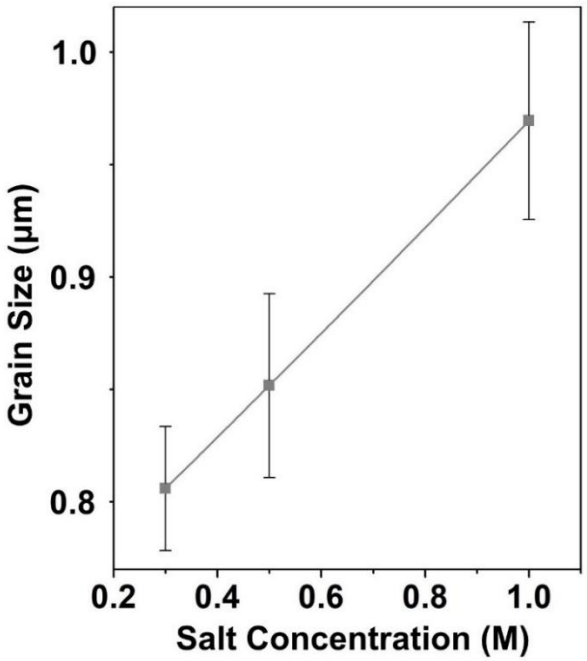

Figure S7. Comparison of crystalline domain sizes of the rhombic dodecahedron microcrystals formed from a bcc superlattice using 15-nm nanoparticles and a six base-long sticky end linker at different salt concentrations (0.3, 0.5, and 1 M NaCl). Williamson-Hall analysis was used to deconvolute peak broadening arising from grain size.

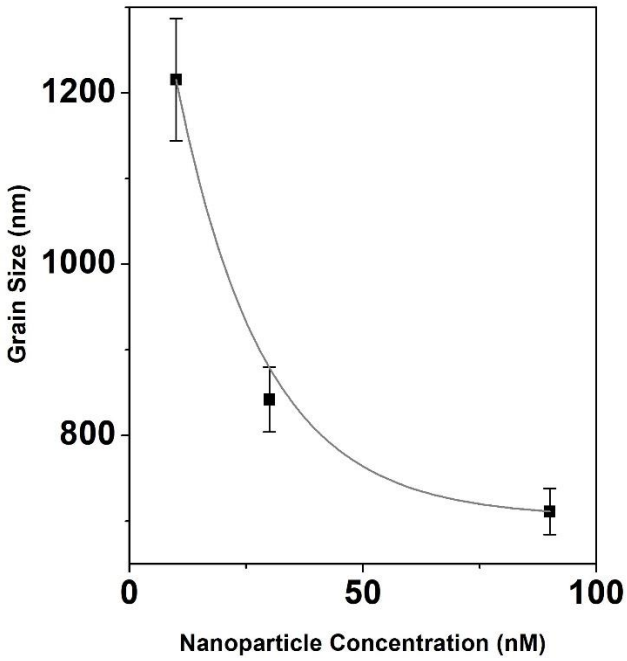

Figure S8. Williamson-Hall analysis of SAXS data was used to measure the change in grain size with nanoparticle concentration.

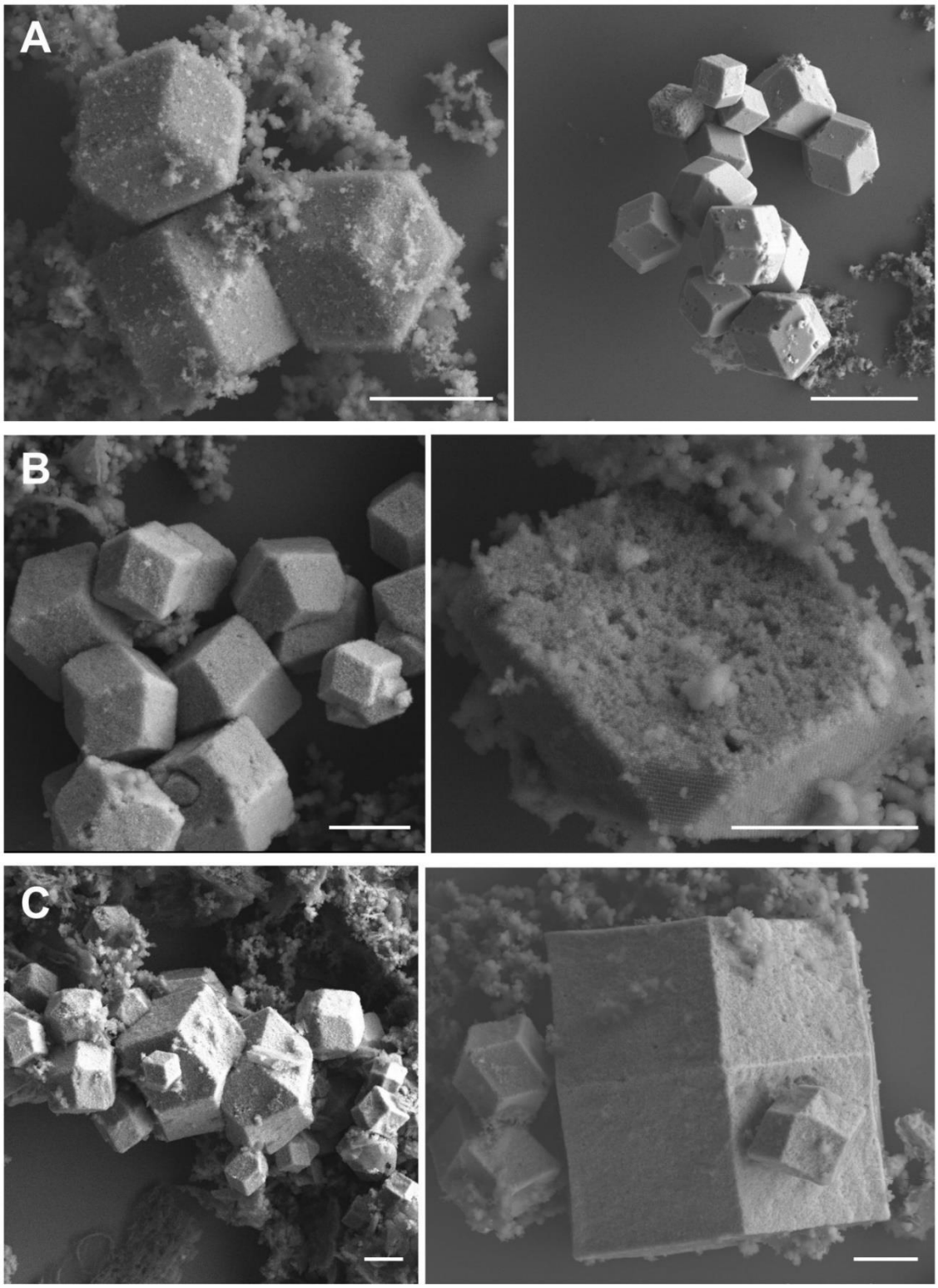

Figure S9. SEM images of the rhombic dodecahedra microcrystals formed from a bcc superlattice using 15-nm nanoparticles and a six base-long sticky end linker at (A) 0.3, (B) 0.5, and (C) 1 M NaCl. A similar trend of increasing crystal size with salt concentration is observed. Some crystals were broken during the silica encapsulation process. Scale bars are 2 μm.

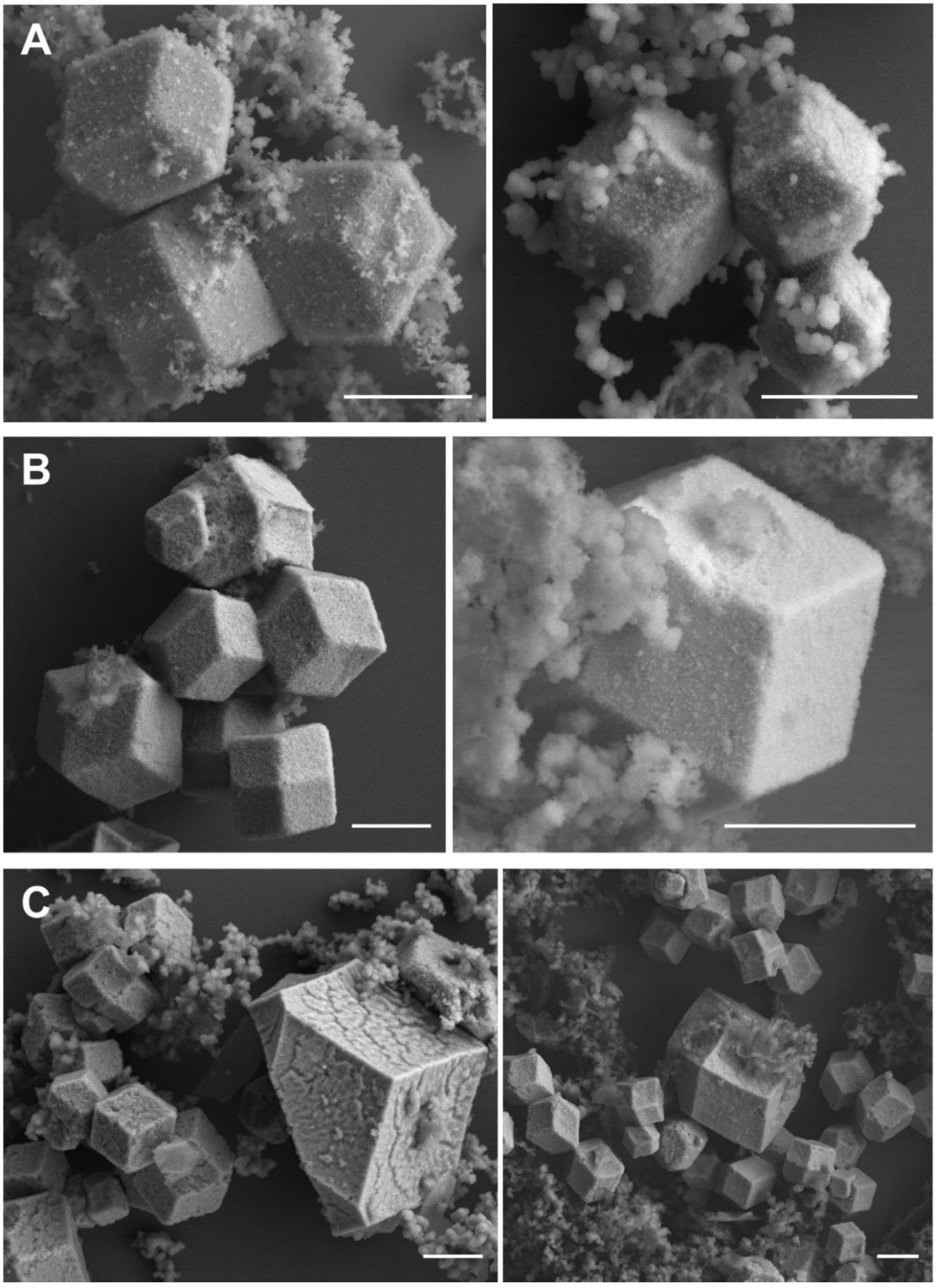

Figure S10. Additional SEM images of the rhombic dodecahedra microcrystals formed from a bcc superlattice using 15-nm nanoparticles and a seven base-long sticky end linker at (A) 0.3, (B) 0.5, and (C) 1 M NaCl. Scale bars are 2 μm.

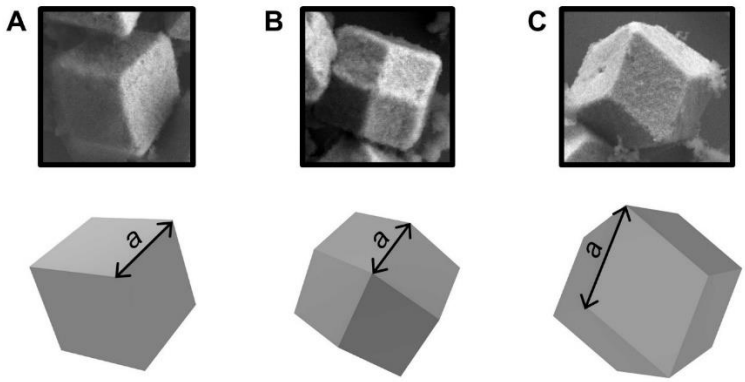

Figure S11. Size distribution determination of microcrystals using SEM. SEM images of rhombic dodecahedron microcrystals viewed from various orientations. Three different orientations are observed. A schematic representation of each crystal orientation is shown on the bottom of each SEM image. Microcrystals that were not sitting in any of shown orientations were not used for size distribution analysis. For *a* values that are measured for the cases (**A**), (**B**), and (**C**) in 2D projections, appropriate length corrections were performed to minimize measurement errors.

Table S2. Length Corrections for Rhombic Dodecahedron Microcrystals in Different Orientations.

System	2D Projection Correction (a*)	Longest Length (With Correction)
A	*a*/cos(60.5°)	2*a**
B	*a*/cos(35.26°)	2*a**
C	*a*	2*a**

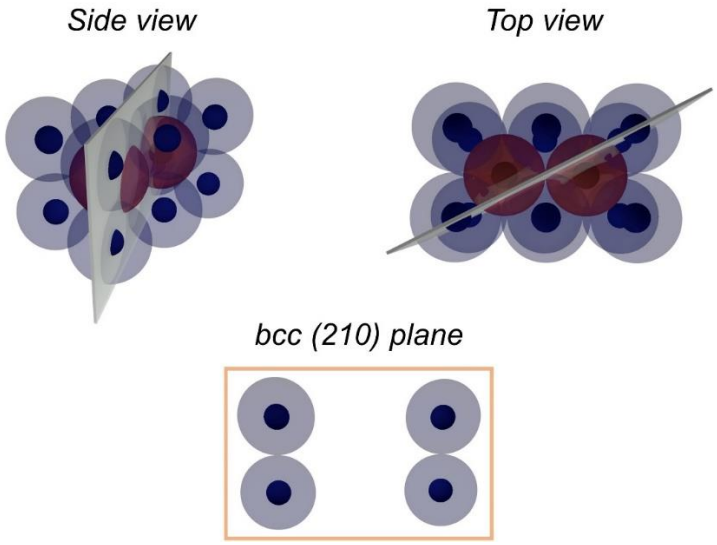

Figure S12. A schematic representation of a bcc (210) plane corresponding to Fig. 3. This figure is shown to clarify which plane of a bcc unit cell is analyzed using SAD. The side and top views of the (210) plane in bcc lattices are shown for clarity.

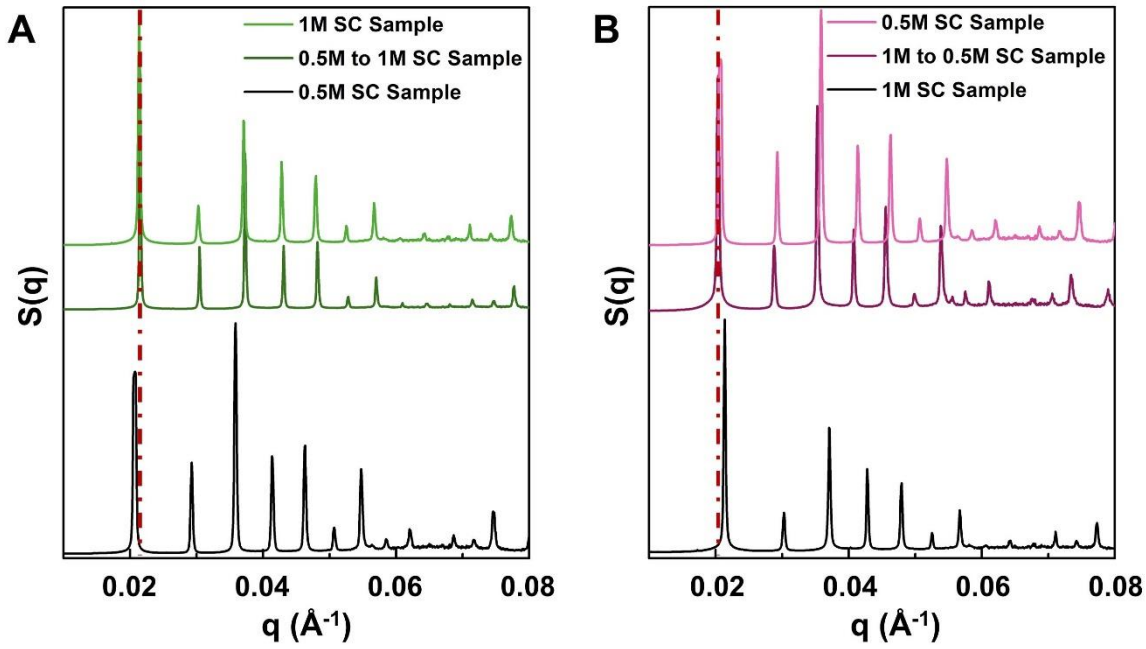

Figure S13. (**A**) SAXS patterns of microcrystals assembled in a buffer at a salt concentration of 1 M, followed by transfer to a buffer at 0.5 M NaCl. (**B**) SAXS patterns of microcrystals assembled in a buffer at a salt concentration of 0.5 M, followed by transfer to a buffer at 1 M NaCl.

References

1. Auyeung, E.; Li, T. I. N. G.; Senesi, A. J.; Schmucker, A. L.; Pals, B. C.; de la Cruz, M. O.; Mirkin, C. A., DNA-mediated nanoparticle crystallization into Wulff polyhedra. *Nature* **2014,** *505*, 73-77.
2. Zwanikken, J. W.; Guo, P.; Mirkin, C. A.; de la Cruz, M. O., Local ionic environment around polyvalent nucleic acid-functionalized nanoparticles. *J. Phys. Chem. C* **2011,** *115*, 16368-16373.
3. Seo, S. E.; Li, T.; Senesi, A. J.; Mirkin, C. A.; Lee, B., The role of repulsion in colloidal crystal engineering with DNA. *J. Am. Chem. Soc.* **2017,** *139* (46), 16528-16535.
4. Li, T. I. N. G.; Sknepnek, R.; Macfarlane, R. J.; Mirkin, C. A.; de la Cruz, M. O., Modeling the crystallization of spherical nucleic acid nanoparticle conjugates with molecular dynamics simulations. *Nano Lett.* **2012,** *12*, 2509-2514.
5. Hinckley, D. M.; Freeman, G. S.; Whitmer, J. K.; De Pablo, J. J., An experimentally-informed coarse-grained 3-site-per-nucleotide model of DNA: Structure, thermodynamics, and dynamics of hybridization. *J. Chem. Phys.* **2013,** *139*, 10B604_1.
6. Hinckley, D. M.; de Pablo, J. J., Coarse-grained ions for nucleic acid modeling. *J. Chem. Theory Comput.* **2015,** *11*, 5436-5446.
7. Li, Y.; Girard, M.; Shen, M.; Millan, J. A.; de la Cruz, M. O., Strong attractions and repulsions mediated by monovalent salts. *Proc. Natl. Acad. Sci.* **2017,** *114*, 11838-11843.
8. Fennell, C. J.; Gezelter, J. D., Is the Ewald summation still necessary? Pairwise alternatives to the accepted standard for long-range electrostatics. *J. Chem. Phys.* **2006,** *124*, 234104.
9. Anderson, J. A.; Lorenz, C. D.; Travesset, A., General purpose molecular dynamics simulations fully implemented on graphics processing units. *J. Comput. Phys.* **2008,** *227*, 5342-5359.
10. Glaser, J.; Nguyen, T. D.; Anderson, J. A.; Lui, P.; Spiga, F.; Millan, J. A.; Morse, D. C.; Glotzer, S. C., Strong scaling of general-purpose molecular dynamics simulations on GPUs. *Comput. Phys. Commun.* **2015,** *192*, 97-107.

11. O'Brien, M. N.; Girard, M.; Lin, H.-X.; Millan, J. A.; de la Cruz, M. O.; Lee, B.; Mirkin, C. A., Exploring the zone of anisotropy and broken symmetries in DNA-mediated nanoparticle crystallization. *Proc. Natl. Acad. Sci.* **2016**, 201611808.
12. Lu, X. J.; Olson, W. K., 3DNA: a software package for the analysis, rebuilding and visualization of three-dimensional nucleic acid structures. *Nucleic Acids Res.* **2003,** *31* (17), 5108-5121.
13. Dhakal, S.; Kohlstedt, K. L.; Schatz, G. C.; Mirkin, C. A.; Olvera de la Cruz, M., Growth dynamics for DNA-guided nanoparticle crystallization. *ACS Nano* **2013,** *7* (12), 10948-10959.
14. Ratke, L.; Voorhees, P. W., *Growth and coarsening: Ostwald ripening in material processing*. Springer Science & Business Media: 2013.
15. Seo, S. E.; Wang, M. X.; Shade, C. M.; Rouge, J. L.; Brown, K. A.; Mirkin, C. A., Modulating the Bond Strength of DNA–Nanoparticle Superlattices. *ACS Nano* **2016,** *10* (2), 1771-1779.
16. Hurst, S. J.; Lytton-Jean, A. K.; Mirkin, C. A., Maximizing DNA loading on a range of gold nanoparticle sizes. *Anal. Chem.* **2006,** *78* (24), 8313-8318.
17. Li, T.; Senesi, A. J.; Lee, B., Small angle X-ray scattering for nanoparticle research. *Chem. Rev.* **2016,** *116* (18), 11128-11180.